# **Huaiqian You**

Department of Mathematics, Lehigh University, Bethlehem, PA 18015

# Quinn Zhang

Department of Mathematics, Lehigh University, Bethlehem, PA 18015

# Colton J. Ross

School of Aerospace and Mechanical Engineering, The University of Oklahoma, Norman, OK 73019

# Chung-Hao Lee

Associate Professor School of Aerospace and Mechanical Engineering, The University of Oklahoma, Norman, OK 73019

# Ming-Chen Hsu

Associate Professor Department of Mechanical Engineering, Iowa State University, Ames. IA 50011

# Yue Yu

Associate Professor, Department of Mathematics, Lehigh University, Bethlehem, PA 18015 e-mail: yuy214@lehigh.edu

# A Physics-Guided Neural Operator Learning Approach to Model Biological Tissues From Digital Image Correlation Measurements

We present a data-driven workflow to biological tissue modeling, which aims to predict the displacement field based on digital image correlation (DIC) measurements under unseen loading scenarios, without postulating a specific constitutive model form nor possessing knowledge of the material microstructure. To this end, a material database is constructed from the DIC displacement tracking measurements of multiple biaxial stretching protocols on a porcine tricuspid valve anterior leaflet, with which we build a neural operator learning model. The material response is modeled as a solution operator from the loading to the resultant displacement field, with the material microstructure properties learned implicitly from the data and naturally embedded in the network parameters. Using various combinations of loading protocols, we compare the predictivity of this framework with finite element analysis based on three conventional constitutive models. From in-distribution tests, the predictivity of our approach presents good generalizability to different loading conditions and outperforms the conventional constitutive modeling at approximately one order of magnitude. When tested on out-of-distribution loading ratios, the neural operator learning approach becomes less effective. To improve the generalizability of our framework, we propose a physics-guided neural operator learning model via imposing partial physics knowledge. This method is shown to improve the model's extrapolative performance in the small-deformation regime. Our results demonstrate that with sufficient data coverage and/or guidance from partial physics constraints, the data-driven approach can be a more effective method for modeling biological materials than the traditional constitutive modeling.

[DOI: 10.1115/1.4055918]

Keywords: operator-regression neural networks, implicit Fourier neural operator (IFNO), data-driven material modeling, heart valve leaflet

#### 1 Introduction

35

39

41

42

46

47

48

49

51

52

For many decades, constitutive models based on continuum mechanics have been commonly employed for modeling the mechanical responses of soft biological tissues. In Ref. [1], the seminal phenomenological constitutive models were developed and later employed for the modeling of soft tissues, including the iris [2], cardiac heart valves [3–5], arterial vessels [6], and the skin [7]. In the constitutive modeling approaches, a strain energy density function is predefined with a specific functional form. Then, the material parameters are calibrated through an inverse method or analytical stress–strain fitting. The descriptive power of these models is often restricted to certain deformation modes/ strain ranges, which might lead to limited predictivity and generalizability [8–10].

To circumvent such a limitation, data-driven computing has been considered in recent years as an alternative for modeling the mechanical response of biological tissues [9,11–13]. Unlike the traditional material identification techniques in constitutive modeling, data-driven approaches directly integrate material identification with the modeling procedures, and hence do not require a predefined constitutive model form. In Ref. [11], a fully convolutional neural network was trained based on synthetic datasets, to

estimate a displacement field of material points in the simulated liver organ. In Ref. [14], Miñano et al. construct the constitutive law for soft tissue damage by solving the system of linear equations consisting of coefficients of shape functions, rather than nonlinear fitting to a predefined model. In Ref. [9], a local convexity data-driven computational framework was developed that couples manifold learning with nonlinear elasticity, for modeling a representative porcine mitral (heart) valve posterior leaflet's stress-strain data. This framework was further extended to an auto-embedding data-driven approach [12] to infer the underlying low-dimensional embedding representation of the material database. In Ref. [13], a neural network was developed to learn the mechanical behavior of porcine and murine skin from biaxial testing data by inferring the relationship between the isochoric strain invariants and the value of strain energy, as well as the strain energy derivatives. Despite these advances, data-driven methods on soft tissue modeling are mostly focusing on the identification of stress-strain and/or energy-strain relationships for a homogenized material model, and are thus not capable to capture the effects of material spatial heterogeneity. For example, the lack of considering the soft tissue heterogeneity could induce large errors in the predictions of tissue displacements and stresses [15].

Alternatively, there has been significant progress in the development of deep neural networks (NNs) for heterogeneous material modeling [16–27]. Among these works, we focus on the neural operator learning approach [22–27], which learns the maps between the inputs of a dynamical system and its state, so that the

72

74

75

77

<sup>&</sup>lt;sup>1</sup>Corresponding author

Manuscript received March 31, 2022; final manuscript received October 4, 2022; published online xx xx, xxxx. Assoc. Editor: Adrian Buganza Tepole.

AQ14

87

88

89

90

91

93

94

95

96

97

98

100

101

102

103

104

105

106

107

108

109

110

111

112

113

114

115

117

118

119

120

121

122

123

124

125

126

127

128

129

130

131

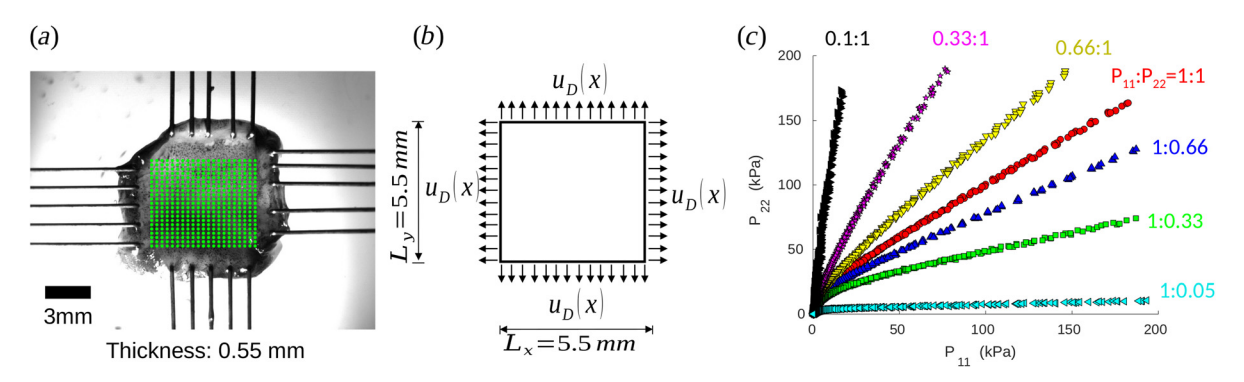


Fig. 1 Problem setup for the proposed data-driven computations: (a) an image of the speckle-patterned porcine TVAL specimen subject to biaxial stretching (the DIC tracking grid is shown in green), (b) schematic of a specimen subject to Dirichlet-type boundary conditions, as the corresponding numerical setting of (a), and (c) first Piola-Kirchhoff stresses  $P_{11}$  versus  $P_{22}$  of seven biaxial tension and constrained uniaxial tension testing protocols, with further details provided in Table 1

network serves as a surrogate for a solution operator. Compared with the classical NNs, the most notable advantage of neural operators is their generalizability to different input instances, rendering a computing advantage on prediction efficiency—once the neural operator is trained, solving for a new instance of the input parameter only requires a forward pass of the network. In Refs. [28-30], neural operators have been successfully applied to modeling the unknown physics law of homogeneous materials. In Refs. [25-27,31], neural operators were used as a solution surrogate for Darcy's flow in a heterogeneous porous medium with a known microstructure field. In our previous work [22], an implicit neural operator architecture, namely, the implicit Fourier neural operator (IFNO), was proposed to model heterogeneous material responses without using any predefined constitutive models or microstructure measurements. In particular, we have investigated the applicability of learning a material model for a latex material directly from digital image correlation (DIC) measurements and show that the learned solution operators substantially outperform the conventional constitutive models such as the generalized Mooney-Rivlin model.

To the best of our knowledge, the neural operator learning approaches have not been applied to soft tissue biomechanics. Moreover, the effectiveness of neural operator learning methods in extrapolation to small and large deformation regimes has yet to be systematically examined. To achieve these goals, in this work we propose to advance the current data-driven methods of soft tissue modeling by extending the neural operator learning approach. In particular, we employ the IFNO to learn the material model from DIC measurements on a representative tricuspid valve anterior leaflet (TVAL) specimen from a porcine heart and assess its predictability on unseen and out-of-distribution loading scenarios. To further improve the generalizability of the proposed framework, we also infuse partial physics knowledge via a soft penalty constraint to obtain a novel physics-guided neural operator learning framework. This method is shown to improve the extrapolative performance of our model in the small deformation regime.

The remainder of this paper is organized as follows. In Sec. 2, we introduce our data-driven computing paradigm based on the neural operator learning method, which integrates material identification, modeling procedures, and material response prediction into one unified learning framework. In particular, a stable deep layer architecture, i.e., the IFNO, is introduced in Sec. 2.2 and incorporated with partial physics knowledge in Sec. 2.3. In Sec. 3, we introduce our experimental setting on a representative TVAL specimen. Four study scenarios, considering different sets of experimental data for model training and predictions, are used to examine the in-distribution and out-of-distribution predictivity of the proposed IFNO method. The effectiveness of the IFNO approach is also compared with finite element simulation results based on three constitutive models. Then, we illustrate the

prediction results of the IFNOs and physics-guided IFNOs, and 133 compared their results with the modeling results based on fitted 134 constitutive models in Sec. 4. Finally, we provide a summary of 135 our achieved goals and concluding remarks in Sec. 5.

137

165

#### 2 An Integrated Learning Framework

In this section, we first formulate the proposed workflow of 138 data-driven material modeling using the operator learning framework and then introduce the deep neural operator model—the 140 IFNO [22]. Next, we propose to further infuse partial physics 141 knowledge via a soft penalty constraint to guide the training and 142 prediction of the neural operators.

2.1 Neural Operator Learning Methods. The main objective tive of this work is to model the mechanical response of a representative soft biological tissue directly from DIC-tracked 146 displacement measurements, without any predefined constitutive 147 model nor knowledge of the tissue microstructure. As depicted in 148 Fig. 1 and Table 1, let us consider a soft biological tissue speci- 149 men that is mounted to a biaxial testing system and deforms under 150 external loading. Denoting the region of interest on this specimen 151 as a 2D domain  $\Omega$ , our aim is to identify the best surrogate operator, that can accurately predict the displacement field u(x),  $x \in \Omega$ , 153 given new and unseen loading scenarios. In this work, we model 154 the tissue mechanical response as a quasi-static and hyperelastic 155 problem for simplicity, so the resultant displacement field can be 156 fully determined by a displacement-type loading applied on the 157 domain boundary  $\partial\Omega$ . Thus, given the Dirichlet-type boundary 158 condition,  $u_D(x)$  for  $x \in \partial \Omega$ , our ultimate goal is to predict the 159 corresponding displacement field u(x),  $x \in \Omega$ .

Mathematically, let K be the unknown differential operator 161 associated with the momentum balance equation which depends 162 on the unknown tissue microstructure and mechanical properties. For a given boundary condition  $u_D(x)$ , the momentum balance equation and boundary conditions are

$$\mathcal{K}[u](x) = 0, \quad x \in \Omega$$

$$u(x) = u_D(x), \quad x \in \partial \Omega$$
(2.1)

Hence, our goal is to provide a surrogate solution operator for 166 Eq. (2.1) as a mapping between any arbitrary  $u_D$  and the corresponding material response u. To this end, we propose to embrace  $\frac{169}{2}$ the descriptive power of NNs, and develop a data-driven neural 170 operator with its input being  $u_D(x)$  and its output being the displacement field u(x), for any  $x \in \Omega$ . Given a collection of 172 observed function pairs  $\{(u_D)_j(x), u_j(x)\}_{j=1}^N$  from DIC measurements, where the input  $\{(\mathbf{u}_D)_j\}, j=1,...,N$  is a sequence of 174 boundary displacement loading and  $\mathcal{G}^{\dagger}[(\mathbf{u}_D)_j](\mathbf{x}) = \mathbf{u}_j(\mathbf{x})$  is the 175

000000-2 / Vol. 00, MONTH 2022

Table 1 Protocols of the mechanical testing on a representative TVAL specimen

Set ID	Experiment protocol	$max(\lambda_1)$	$\max(\lambda_2)$	$max(P_{11})$	$max(P_{22})$	# of samples
1	Biaxial tensions $P_{11}: P_{22} = 1:1$	1.46	1.68	184.1 kPa	165.1 kPa	3921
2	Biaxial tensions $P_{11}: P_{22} = 1:0.66$	1.48	1.63	187.1 kPa	127.8 kPa	3797
3	Biaxial tensions $P_{11}: P_{22} = 1:0.33$	1.52	1.52	186.9 kPa	74.1 kPa	3539
4	Biaxial tensions $P_{11}: P_{22} = 0.66: 1$	1.42	1.72	145.9 kPa	188.2 kPa	4013
5	Biaxial tensions $P_{11}: P_{22} = 0.33:1$	1.32	1.79	77.9 kPa	189.8 kPa	4175
6	Constrained uniaxial in <i>x</i> , $P_{11} : P_{22} = 0.05 : 1$	1.56	1.0	197.9 kPa	10.6 kPa	3539
7	Constrained uniaxial in $y$ , $P_{11}$ : $P_{22} = 1:0.1$	1.0	1.89	17.2 kPa	176.1 kPa	3539

The resultant displacement fields, based on digital image correlation, were used in the data-driven computations ( $P_{11}$  and  $P_{22}$  denote the first Piola–Kirchhoff stresses in the x- and y-directions, respectively, and  $\lambda_1$ ,  $\lambda_2$  are the stretches ratios in these two directions).

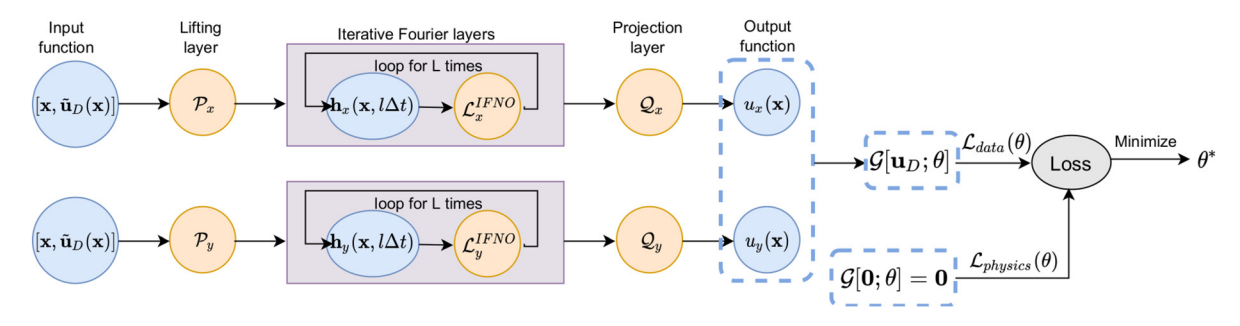


Fig. 2 The architecture of the proposed physics-guided IFNO PG-IFNO, which consists of two subnetworks for the prediction of two displacement field components. Each subnetwork starts from the input  $[x, \tilde{u}_D(x)]$ , then (1) lifts to a high dimensional feature space by the lifting layer  $\mathcal{P}$  and obtains the first hidden layer representation h(x,0); (2) applies L iterative layers; (3) projects the last hidden layer representation  $h(x, L\Delta t)$  back to the target dimension through a shallow network  $\mathcal Q$ . The optimal network parameter  $heta^*$  is obtained by minimizing the hybrid loss function defined as the weighted sum of the data-driven loss,  $\ell_{\text{data}}$ , and the physics constraint loss,  $\ell_{\text{physics}}$ .

corresponding (potentially noisy) displacement field. With neural 177 operator learning, we aim to build an approximation of  $\mathcal{G}'$  by constructing a nonlinear parametric map  $\mathcal{G}[\cdot\,;\,\theta]$  in the form of a NN, 179 for some finite dimensional parameter space  $\Theta$ . Here,  $\theta \in \Theta$  is

180 the set of network architecture parameters to be inferred by solv-

ing the minimization problem

184

185

186

187

189

190

191

192

193

194

195

196

197

199

200

201

202

203

204

206

207

AQ4

$$\min_{\theta \in \Theta} \sum_{j=1}^{N} ||\mathcal{G}[(\boldsymbol{u}_D)_j; \quad \theta](\boldsymbol{x}) - \boldsymbol{u}_j(\boldsymbol{x})||_{L^2(\Omega)}^2$$
 (2.2)

In this context, we have formulated the soft tissue response modeling problem as learning the solution operator  $\mathcal{G}$  of an unknown PDE system from the DIC data.

Thus, our goal is to provide a neural operator, i.e., an approximated solution operator  $\mathcal{G}[\cdot;\theta]: u_D \to u$ , that delivers solutions of Eq. (2.1) for any input  $u_D$ . Compared with the classical PDE solvers and the NN approaches, this is a more challenging task for several reasons. First, in contrast to the classical NN approaches where the solution operator is parameterized between finite dimensional Euclidean spaces [32-36], the neural operators are built as mappings between infinite dimensional spaces [25,27,37]. Second, for every new instance of material microstructure and/or loading scenario f, the neural operators require only a forward pass of the network, which implies that the optimization problem (2.2) only needs to be solved once and the resulting NN can be utilized to solve for new and unseen loading scenarios. This property is in contrast to the classical numerical PDE methods [38–40] and some machine learning approaches [41–45], where the optimization problem needs to be solved for every new instance of the input parameter of a known governing law. Finally, of fundamental importance is the fact that the neural operators can find solution maps regardless of the presence of an underlying PDE and only require the observed data pairs  $\{((\boldsymbol{u}_D)_j, \boldsymbol{u}_j)\}_{j=1}^N$ . Therefore, the neural operator learning approach is particularly promising when the mechanical responses are provided by experimental

measurements, such as the displacement tracking data from DIC 208 considered in this paper.

2.2 Implicit Fourier Neural Operators. To provide an efficient, deep, and stable integral neural operator for the solution 211 operator learning problem discovered above, we employ the 212 IFNOs [22]. IFNOs stem from the idea of modeling the solution 213 operator as a fixed point equation that naturally mimics the solu- 214 tion procedure for the displacement/damage fields in materials 215 modeling. The increment between neural network hidden layers is 216 modeled as an integral operator, which is directly parameterized 217 in the Fourier space to facilitate the fast Fourier transformation 218 and accelerated learning techniques for deep networks. As shown 219 in Ref. [22], by learning the material responses directly from data, 220 the material microstructure and properties are learned implicitly 221 and embedded naturally in the network parameters, enabling the 222 prediction of the material displacement for unseen loading 223 conditions.

Figure 2 depicts the NN architecture employed in this work. Two IFNOs are built to predict  $u_x(x)$  and  $u_y(x)$ , the x and y components of the displacement field, respectively. For each IFNO, 227 the input is a vector function f(x) on  $\Omega$  that contains information 228 from x and  $u_D(x)$ . Here, we notice that the displacement boundary 229 loading  $u_D(x)$  is only defined on  $\partial\Omega$ . To make it well-defined on 230 the whole domain, we employ the zero-padding strategy proposed in Ref. [31], namely, defining  $f(x) := [x, \tilde{u}_D(x)]$  where

$$\tilde{\mathbf{u}}_{D}(\mathbf{x}) = \begin{cases} \mathbf{u}_{D}(\mathbf{x}), & \text{if } \mathbf{x} \in \partial \Omega \\ 0, & \text{if } \mathbf{x} \in \Omega \backslash \partial \Omega \end{cases}$$
 (2.3)

Then, we lift the input  $f(\cdot)$  to a representation (feature)  $h(\cdot,0)$  of 233 dimension d, that corresponds to the first network layer. For the  $\frac{235}{2}$ consistency of notation, we label the first argument of h as 236 the space (the set of nodes) and the second argument as the time 237 238 (the set of layers) and define the first network layer as

Journal of Biomechanical Engineering

MONTH 2022, Vol. 00 / 000000-3

261

262

263

267

268

269

270

277

278

279

280

281

282

283

$$h(x,0) = \mathcal{P}[f](x) := Pf(x) + p$$

where  $P \in \mathbb{R}^{d \times 4}$  and  $\mathbf{p} \in \mathbb{R}^d$  are trainable parameters. 239

241 Second, we denote the *l*th network representation by  $h(x, l\Delta t)$ , and formulate the NN architecture in an iterative manner: 242  $h(\cdot,0) \to h(\cdot,\Delta t) \to h(\cdot,2\Delta t) \to \cdots \to h(\cdot,T)$ , where  $h(\cdot,j\Delta t)$ ,  $j = 0, ..., L := T/\Delta t$ , is a sequence of functions representing the features at each hidden layer, taking values in  $\mathbb{R}^d$ . Here, l=0 (or equivalently, t=0) denotes the first hidden layer, whereas t= $L\Delta t = T$  corresponds to the last hidden layer. In particular, the layer update rule in the IFNOs writes

$$h(x, (l+1)\Delta t) = \mathcal{L}^{\text{IFNO}}[h(x, l\Delta t)]$$

$$:= h(x, l\Delta t) + \Delta t \sigma(Wh(x, l\Delta t) + \mathcal{F}^{-1}[\mathcal{F}[\kappa(\cdot; v)] \cdot \mathcal{F}[h(\cdot, l\Delta t)]](x) + c)$$

Here,  $\mathcal{F}$  and  $\mathcal{F}^{-1}$  denote the Fourier transform and its inverse, respectively. In practice,  $\mathcal F$  and  $\mathcal F^{-1}$  are computed using the fast 249 Fourier transformation and its inverse to each component of h sep-251 arately, with the highest modes truncated and keeping only the first k modes. Also,  $\mathbf{c} \in \mathbb{R}^d$  defines a constant bias,  $W \in \mathbb{R}^{d \times d}$  is the weight matrix, and  $\mathcal{F}[\kappa(\cdot; \mathbf{v})] := R \in \mathbb{C}^{d \times d \times k}$  is a circulant 252 253 254 matrix that depends on the convolution kernel  $\kappa$ . We further 255 define  $\sigma$  as the activation function, which is chosen to be the pop-256 ular rectified linear unit (ReLU) function [46]. Here we note that 257 the definition of t stems from the relationship established between 258 the network update and a time stepping scheme, which enables 259 the employment of the accelerated training strategy for the NN in the deep layer limit. 260

Third, the output  $u_x(x)$  or  $u_y(x)$  is obtained through a projection layer. Taking the IFNO for the prediction of  $u_x(x)$ , for example, we project the last hidden layer representation  $h(\cdot,T)$  as

$$u_x(\mathbf{x}) = \mathcal{Q}[\mathbf{h}(\cdot,T)](\mathbf{x}) := Q_2 \sigma(Q_1 \mathbf{h}(\mathbf{x},T) + \mathbf{q}_1) + \mathbf{q}_2$$

Here,  $Q_1 \in \mathbb{R}^{d_Q \times d}$ ,  $Q_2 \in \mathbb{R}^{1 \times d_Q}$ ,  $q_1 \in \mathbb{R}^{d_Q}$ , and  $q_2 \in \mathbb{R}$  are the 265 266 trainable parameters.

Denoting the parameters and the corresponding operators associated with  $u_x$  and  $u_y$  with the subscripts x and y, respectively, the vanilla version of our neural operator learning architecture without physics constraints (which will be denoted as IFNO in the following context, with a slight abuse of notation) is written as:

$$egin{aligned} \mathcal{G}[u_D; heta](x) &:= [\mathcal{Q}_x \circ (\mathcal{L}_x^{ ext{IFNO}})^L \circ \mathcal{P}_x[f](x) \ \mathcal{Q}_y \circ (\mathcal{L}_y^{ ext{IFNO}})^L \circ \mathcal{P}_y[f](x)] \ pprox [u_x(x), u_y(x)] &= u(x) \end{aligned}$$

Note that the trainable parameters are collected in  $\theta :=$  $\{P_x, \boldsymbol{p}_x, (Q_1)_x, (Q_2)_x, (\boldsymbol{q}_1)_x, (\boldsymbol{q}_2)_x, \boldsymbol{c}_x, W_x, R_x, P_y, \boldsymbol{p}_y, (Q_1)_y, (Q_2)_y, (\boldsymbol{q}_1)_y, (q_2)_y, \boldsymbol{c}_y, W_y, R_y\},$  obtained in the vanilla IFNO by minimizing the data-driven loss only

$$\begin{aligned} \boldsymbol{\theta}^* &= \underset{\boldsymbol{\theta} \in \Theta}{\operatorname{argmin}} \ \mathcal{L}_{\operatorname{data}}(\boldsymbol{\theta}), \ \text{ where} \\ \mathcal{L}_{\operatorname{data}}(\boldsymbol{\theta}) &:= \sum_{i=1}^N \lvert\lvert \mathcal{G}[(\boldsymbol{u}_D)_j; \boldsymbol{\theta}](\boldsymbol{x}) - \boldsymbol{u}_j(\boldsymbol{x}) \rvert\rvert_{L^2(\Omega)}^2 \end{aligned} \tag{2.4}$$

Further, as the layer becomes deep  $(\Delta t \to 0)$ , the iterative architecture of the IFNOs can be seen as an analog of discretized ordinary differential equations (ODEs). This allows us to exploit the shallow-to-deep learning technique [22,37,47,48]. Specifically, using the optimal network parameters  $\theta^*$  obtained by training an IFNO of depth L, we initialize the (deeper)  $\tilde{L}$ -layer network. As such, the optimal parameters learned on shallow networks are considered as (quasi-optimal) initial guesses for the deeper networks—accelerating the training for deeper NNs.

2.3 Physics-Guided Neural Operators. So far, the neural 285 operator model introduced above fully relies on the data, and 286 hence its predictions may not be consistent with the underlying 287 physical principles. For instance, with the quasi-static and hyperelastic assumption of our model, the specimen has no permanent 289 deformation. In other words, if there is no loading applied to the 290 tissue (i.e., the specimen is at rest), we should observe a zero dis-291 placement field in the specimen. However, this is generally not 292 guaranteed in a fully data-driven neural operator model.

In this work, we aim to further leverage the neural operator 294 learning architecture by imposing the underlying physical laws 295 via soft penalty constraints during model training. In particular, 296 considering a specimen at rest, the no-permanent-deformation 297 assumption implies that zero loading should lead to zero displace- 298 ment, i.e.,  $\mathcal{G}'[0] = 0$ . To enable the neural operator predictions to 299 be consistent with this physical constraint, we propose a physics- 300 guided neural operator model that minimizes the residual of the 301 above physical law together with the fitting loss from the data. 302 This is achieved by solving the following minimization problem 303 with a hybrid loss function:

$$\theta^* = \underset{\theta \in \Theta}{\operatorname{argmin}} \ \mathcal{L}_{\operatorname{data}}(\theta) + \gamma \mathcal{L}_{\operatorname{physics}}(\theta) \tag{2.5}$$

304

315

316

where the data-driven loss  $\mathcal{L}_{data}$  is defined in Eq. (2.4), and the 306 physics constraint loss  $\mathcal{L}_{physics}$  is defined as

$$\mathcal{L}_{\text{physics}}(\theta) := ||\mathcal{G}[\mathbf{0}; \theta](\mathbf{x})||_{L^{2}(\Omega)}^{2}$$
 (2.6)

Here,  $\gamma > 0$  is a penalty parameter to enforce the zero deformation 309 state for material subject to zero loading. Thus, the physics- 310 guided neural operator is anticipated to improve the prediction 311 performance in the small deformation regime. In the following, 312 we will denote this model as the physics-guided IFNO, or the PG-IFNO, in short. 314

## 3 Application to Tissue Biomechanics of the Heart Valve Leaflet

We now consider the problem of learning the material response 317 of a TVAL specimen from displacement measurements based on 318 DIC tracking. In this problem, the constitutive equations and 319 material microstructure are both unknown, and the dataset has 320 unavoidable measurement noise. To demonstrate the efficacy of 321 the proposed IFNOs in conjunction with the physics-based enrichment, we further compared our method against three conventional 323 approaches that use constitutive modeling with parameter fittings. 324 The code and dataset have been publicly released at the following 325 link.2

3.1 Tissue Preparation and Mechanical Testing. In this 327 section, we first introduce the experimental specimen and data 328 acquisition procedure. In brief, we followed our previously established biaxial testing procedure, including acquisition of a healthy 330 porcine heart and retrieval of the TVAL [49,50]. We then sec- 331 tioned the leaflet tissue into a square specimen and measured the 332 thickness using an optical measuring system (Keyence, Itasca, 333 IL). Afterward, we applied a speckling pattern to the tissue sur- 334 face using an airbrush and black paint [51–53]. The painted specimen was then mounted to a biaxial testing device (Bio-Tester, 336 CellScale, Waterloo, ON, Canada) with an effective testing area 337 of  $9 \times 9$  mm for the following tissue characterizations (Fig. 1(a)).

First, we performed a preconditioning protocol in which the 339 specimen was subjected to ten cycles of biaxial loading and 340 unloading that targeted a first Piola-Kirchhoff stress of 150 kPa to 341 emulate the valve's in vivo functioning conditions [54]. Then, we 342 performed seven protocols of displacement-controlled testing to 343

00000-4 / Vol. 00, MONTH 2022

<sup>2</sup>https://github.com/fishmoon1234/IFNO-tissue

345

346

347

348

349

351

352

353

354

355

356

357

358

359

360

361

362

363

364

365 366

367

368

369

370

373

374

375

376

377

378

379

381

382

383

385

386

387

388

389

401

target various biaxial stresses:  $P_{11}:P_{22}=1:1$ , 1:0.66, 1:0.33, 0.66:1, 0.33:1, 0.05:1, 1:0.1, with the last two protocols for constrained uniaxial stretching in x and y (Fig. 1(c) and Table 1). Here,  $P_{11}$  and  $P_{22}$  denote the first Piola–Kirchhoff stresses in the x- and y-directions, respectively. Each stress ratio was performed for three loading/unloading cycles. Throughout the test, images of the specimen were captured by a CCD camera, and the load cell readings and actuator displacements were recorded at 5 Hz. Due to the use of displacement-controlled testing, we observed mild deviations from the target stresses (see Table 1).

After testing, the acquired images were analyzed using the DIC module of the Bio-Tester's software. A  $5.5 \times 5.5$  mm domain in the central region of the TVAL specimen was selected since the speckling pattern was more uniform and could yield more reliable node tracking (see Figs. 1(a) and 1(b)). The pixel coordinate locations of the DIC-tracked grid were then exported for use in the subsequent study scenarios. Based on the tracked coordinates, we constructed two numerical testing datasets: (i) an original dataset obtained directly from the experimental measurements, and (ii) a smoothed dataset where moving least-squares (MLS) smoothing was performed for the nodal displacements.

To generate the displacement fields  $\boldsymbol{u}^{\text{original}}(\boldsymbol{x})$  for the original samples, we subtracted each material point location with its initial location on the first sample of each protocol, and the boundary displacement was obtained by enforcing  $\boldsymbol{u}^{\text{original}}(\boldsymbol{x})$  on the boundary nodes. Next, to construct the smoothed samples for the  $i^{\text{th}}$  material point,  $\boldsymbol{x}_i = (x_i, y_i)$ , we employed a two-dimensional MLS shape function  $\Psi_i$  to reconstruct the smoothed displacement field:  $\boldsymbol{u}^{\text{smooth}}(x_i, y_i) = \sum_{k=1}^{NP} \Psi_k(x_i, y_i) \boldsymbol{u}^{\text{original}}(x_k, y_k)$ , based on the unsmoothed displacement vector of the NP points in the neighborhood of  $\boldsymbol{x}_i$ . For further details regarding the MLS shape function and the smoothing procedure, we refer interested readers to Refs. [22], [55], and [56]. Both the smoothed and the original datasets have 26,523 total time instants (samples), denoted as  $\mathcal{D}_{\text{smooth}}^{\text{smooth}} = \{(\boldsymbol{u}_D)_j^{\text{smooth}}, \boldsymbol{u}_j^{\text{smooth}}\}_{j=1}^{26,523}$  and  $\mathcal{D}_{\text{original}}^{\text{original}} = \{(\boldsymbol{u}_D)_j^{\text{original}}, \boldsymbol{u}_j^{\text{sooth}}\}_{j=1}^{26,523}$ , respectively. Finally, to create a structured grid for the proposed IFNOs, we further applied a cubic spline interpolation to the displacement field on a structured 21 × 21 node grid.

3.2 Baseline: Constitutive Modeling. As the baseline method for comparisons with the proposed neural operator learning methods, we considered a constitutive modeling approach using parameter fitting to the experimental stress–stretch data. In particular, for comparisons with the IFNO approach, we employed three models for the planar stress–strain behavior of the tissue: (i) a Fung-type model, (ii) an invariant-based model, and (iii) a structure-informed model. The Fung-type model was considered with the strain energy density function given by

$$\psi = \frac{c}{2} \left[ \exp\left(a_1 E_{11}^2 + a_2 E_{22}^2 + 2a_3 E_{11} E_{22}\right) - 1 \right]$$

where c,  $a_1$ ,  $a_2$ , and  $a_3$  are the model parameters to be determined, and  $E_{11}$ ,  $E_{22}$  are the principle Green–Lagrange strains in the x-and y-directions, respectively.

The invariant-based model was chosen as the Lee–Sacks form [8,57,58], with the strain energy density function defined as

$$\psi = \frac{c_0}{2}(I_1 - 3) + \frac{c_1}{2} \left[ w \exp\left(c_2(I_1 - 3)^2\right) + (1 - w)\exp\left(c_3(I_4 - 1)^2\right) - 1 \right]$$

Herein,  $c_i$  (i = 0, 1, 2, 3) and w are the model parameters to be determined,  $w \in [0, 1]$  denotes the material anisotropy, and  $I_1 = tr(\mathbf{C})$  and  $I_4 = \mathbf{m} \cdot \mathbf{Cm}$  are the invariant and pseudo-invariant of the right Cauchy–Green deformation  $\mathbf{C} = \mathbf{F}^T \mathbf{F}$ , respectively. In this study, we consider the direction of the collagen fibers in the reference configuration to be in the circumferential direction (i.e.,  $\mathbf{m} = [1, 0, 0]^T$ ).

Finally, for the structure-informed model, we use a simplified 402 ensemble fiber stress–strain relationship, along with a neo-403 Hookean nonfibrous ground matrix [9,10,59,60], with the strain 404 energy density function 405

$$\psi = \psi_{\rm m} + \psi_{\rm ens} = \frac{\mu_{\rm m}}{2} (I_1 - 3) + p(J - 1) + \int_{-\pi/2}^{\pi/2} \Gamma(\theta) \psi_{\rm f} [E_{\rm f}(\theta)] d\theta$$

where  $\mu_{\rm m}$  is the neo-Hookean stiffness and p is the penalty term to enforce tissue incompressibility  $J=\det(\mathbf{F})=1$  that can be analytically determined by further applying the plane-stress condition [59],  $E_{\rm f}=\mathbf{N}^{\rm T}(\theta)\mathbf{E}\mathbf{N}(\theta)$  is the fiber strain along  $\mathbf{N}(\theta)=410$   $\left[\cos(\theta),\sin(\theta),0\right]^{\rm T},\mathbf{E}=(\mathbf{C}-\mathbf{I})/2$  is the Green-Lagrange strain, and  $\mathbf{I}$  is the identity tensor. For the fiber stress-strain behavior, we used an exponential model with a terminal stiffness for numerical stability

$$S_{\mathrm{f}} = \frac{\partial \psi_{\mathrm{f}}}{\partial E_{\mathrm{f}}} = \begin{cases} c_0[\exp(c_1 E_{\mathrm{f}}) - 1], & \text{for } E_{\mathrm{f}} \leq E_{\mathrm{ub}} \\ c_0[\exp(c_1 E_{\mathrm{ub}}) - 1] \\ + c_0 c_1 \exp(c_1 E_{\mathrm{ub}})(E_{\mathrm{f}} - E_{\mathrm{ub}}), & \text{for } E_{\mathrm{f}} > E_{\mathrm{ub}} \end{cases}$$

where  $c_0$  and  $c_1$  are the material parameters and  $E_{\rm ub}$  is threshold 415 fiber strain for the transition to a linear fiber tangent modulus. 416 Finally, we used a Gaussian distribution function, with zero mean 417 and fiber dispersion of  $\sigma$ , for  $\Gamma_{\theta}$ . Thus, for the structure-informed 418 model there are four parameters to be determined from optimization:  $\mu_{\rm m}$ ,  $c_0$ ,  $c_1$ , and  $\sigma$ , whereas  $E_{\rm ub}$  is precalculated as the strain 420 corresponding to a predetermined stress threshold value of 421 10 MPa for a given pair of  $c_0$  and  $c_1$ .

In this work, constitutive model parameters were obtained by 423 nonlinear least-squares fitting to the biaxial stress-stretch data for 424 the training samples. In brief, the first Piola-Kirchhoff stresses in the x- and y-directions were determined using the specimen thick-  $\frac{426}{100}$ ness  $L_z$ , the undeformed edge lengths  $L_x$  and  $L_y$ , and the measured 427 forces  $F_x$  and  $F_y$ :  $P_{11} = F_x/L_yL_z$  and  $P_{22} = F_y/L_xL_z$ . The two 428 stretches were calculated as the ratio of the deformed to the undeformed edge lengths. To obtain the optimal parameters for the dif- 430 ferent model, differential evolution optimization was employed 431 that minimizes the residual mean squared errors in the stress 432 between the experimental data and model prediction [61]. Finally, 433 using the determined model parameters, finite element simulation 434 was performed in Abaqus [62] with the DIC-tracked nodal displacements prescribed as boundary displacement conditions. The 436 relative errors of displacement fields were then evaluated by comparing the finite element solution and the DIC-based measurements. In the following, we will refer to these baseline approaches 439 as the "Fung model" method, the "invariant-based" method, and 440 the "structure-informed" method.

3.3 Numerical Study Scenarios. Based on the seven 442 mechanical testing protocols listed in Table 1, four study scenarios are considered to evaluate the interpolative and extrapolative 444 performances of the proposed neural operator learning methods. 445 In each study scenario, a subset of the samples was selected to 446 form the training set and to obtain the optimal neural operator by 447 solving (2.2) and (2.6). Then, the displacement field predictions 448 were made for the remaining samples and the results were compared with the ground-truth displacement fields from the DIC measurements, to evaluate the predictivity and generalizability of our proposed methods. Due to the relatively large number of sam- 452 ples, in constitutive modeling approach, it is generally intractable 453 to perform finite element analysis for all 26,523 samples. To 454 reduce the computational cost, although we train both models on 455 samples from all cycles, we only evaluate the training and testing 456 errors for samples in the first loading/unloading cycle of each pro- 457 tocol for the three constitutive modeling approaches. Then, we 458

Journal of Biomechanical Engineering MONTH 2022, Vol. 00 / 000000-5

461

462

463

464

465

467

468

469

470

471

472

474

475

476

477

478

479

480

481

483

484

485

486

488

489

490

492

493

494

495

497

498

500

501

502

504

505

507

508

510

511

512

514

515

517

518

520

AQ6

considered the averaged relative error of displacement,  $||u_{\text{pred},j} - u_j||_{L^2(\Omega)} / ||u_j||_{L^2(\Omega)}$ , as the error metric, so as to provide a fair comparison between the constitutive modeling and our neural operator learning approaches. Here,  $u_j$  denotes the jth sample from the DIC measurement, and  $u_{pred,j}$  is the prediction from either the neural operator or the corresponding baseline constitutive model for this sample.

3.3.1 Study 1. We mixed all samples from all seven protocols, randomly selected 83% of samples for training, and used the remaining for validation (10% of samples) and testing (7% of samples). In this scenario, we ensured that the boundary conditions of the samples in the testing set are inside the training region. Therefore, with this study, we aimed to investigate the indistribution predictivity of the proposed method. With this study, we not only investigate the performance of the proposed approach in in-distribution learning tasks but also study the required amount of training data by demonstrating the errors when using different numbers of (randomly) selected training samples.

Study 2. For this study, we employed protocols 1, 2, and 4 for training and protocols 3, 5, 6, and 7 for testing. In this study and the two studies below, the samples from the second loading/ unloading cycle of testing protocols are employed as the validation dataset for the purpose of hyperparameter tuning, while the first cycle is reserved as the test dataset. We notice that the testing protocols are not covered in any of training sets, and they have smaller maximum tensions compared with the training sets. Hence, with this study, we aimed to investigate the performance of the proposed IFNO methods for predicting the out-of-distribution material responses in the small deformation regime.

3.3.3 Study 3. We used protocols 1, 6, and 7 for training and protocols 2–5 for testing. The protocols considered in testing were not covered in any of the training protocols, although the deformation range of the testing protocols may fall inside the range of the training ones. Hence, we attempted to illustrate the out-of-distribution prediction on the intermediate deformation regime.

3.3.4 Study 4. We used protocols 2–7 for training, and protocol 1 for prediction. We notice that the equibiaxial tension protocol  $(P_{11}: P_{22} = 1:1)$  is not covered in any of other sets, and protocol 1 exhibits the largest maximum tensions among all the sets. Hence, with this study, we aimed to investigate the out-ofdistribution predictivity in the large deformation regime of the proposed method.

#### **Results and Discussions**

In this section, we illustrate the performance of the proposed neural operator learning approaches. All our numerical experiments were performed on a machine with a 2.8 GHz 8-core CPU and a single Nvidia RTX 3060 GPU, using a Pytorch implementation modified from the package provided in Ref. [27]. The optimization was performed with the Adam optimizer. For all IFNOs, we set the dimension of h as d = 16 and the number of truncated Fourier modes as  $k = 8 \times 8$ , with L = 12 hidden layers. The network was trained with the shallow-to-deep training procedure: we initialized the L- layer network parameters from the (L/2)layer IFNOs model. For each depth L, we trained the network for 1000 epochs with a learning rate of  $3 \times 10^{-3}$ , then decreased the learning rate with a ratio of 0.5 every 100 epochs. For all PG-IFNOs we took the penalty parameter  $\gamma = 1.0$ , although we noted that this parameter can be further hand-tuned or optimized to potentially achieve a better performance.

**4.1 Study 1: In-Distribution Prediction.** To verify the model's predictivity for in-distribution learning tasks, in this study we randomly selected 83% of the samples of all protocols to form the training set and then built the vanilla IFNO model and the three baseline constitutive models based on this common training set.

Figure 3 (top) shows the relative displacement errors when using 522 different amounts of training samples, and the samplewise errors for each model are provided in Fig. 3 (bottom). When comparing the results between the original dataset and the smoothed dataset, one can observe that their samplewise errors present a similar 526 trend, while the smoothing procedure slightly improves the prediction accuracy for both the IFNO and three baseline models. Probably unsurprisingly, from the left of Fig. 3 (top), one can see that the accuracy of the IFNO improves when using more training samples. In particular, the test error decreases with a convergence 531 rate of around  $O(N^{-0.34})$ , when the training dataset size, N, 532 increases. With only 45 samples, the IFNO achieves a comparable 533 accuracy as the three constitutive models trained on all 22,000 534 samples. When using all 22,000 measurements in both models, the IFNO outperforms the conventional constitutive modeling approaches by around one order of magnitude, on both the original and smoothed datasets. To provide further insights into this 538 comparison, in Fig. 4 we visualized both the x- and ydisplacement solutions and the prediction errors obtained with the 540 IFNO and the structure-informed model (the best baseline model) on two test samples, which correspond to the large deformation (sample #2) and small deformation (sample #1) representatives, respectively. The structure-informed model, which considered the homogenized stress-strain at one material point (i.e., the center of 545 the specimen) due to limited information about the spatial variation in the stress measurement, failed to capture material heterogeneity and hence exhibited large prediction errors in the interior region of the TVAL specimen domain. This observation confirms the importance of capturing the material heterogeneity and verifies the capability of the IFNOs in heterogeneous material modeling.

4.2 Study 2: Out-of-Distribution Prediction on the Small 553 **Deformation Regime.** In this study, three protocols with the largest tensions (i.e., sets 1, 2, and 4) were used for training, and the other four protocols were used for prediction validation (sets 3, 5, 6, and 7 as listed in Table 1). Since the prediction sets are with a 557 different biaxial loading ratio that is unseen from the training samples, this is an extrapolative learning task in the small deformation 559 region. Figure 5 (*left*) provides the relative displacement errors from all models. One can see that compared with the interpolative prediction task in study 1, the extrapolative predictions are less effective for the neural operator. It was, in particular, noted that for the vanilla IFNO model while the training error was at a relatively low error (i.e., the model still possessed good expressivity in sets 1, 2, and 4), the testing error deteriorates by ten times and reached a similar level to the Fung-type model but slightly higher than invariant-based and structure-informed models. Perhaps unsurprisingly, this observation again verifies the sensitivity of 569 machine learning models in extrapolative tasks (see, e.g., Ref. 570 [9]). As shown in Fig. 5 (*right*), we demonstrate the samplewise 571 errors from the original dataset for each model, and we noticed 572 that the results on the smoothed dataset exhibit a similar trend. One can observe that for the three baseline models, the level of prediction errors is relatively similar for all four testing sets, while large errors are observed in sets 6 and 7 (the sets with the smallest 576 maximum tensions) for the vanilla IFNO model. Those sets are the furthest away from the training set and hence their sample dis- 578 tributions are substantially different from those in the training 579

In this study, we also investigated the performance of the proposed PG-IFNOs. By infusing the no-permanent-deformation constraint, an improvement of the testing error was observed on both 583 original and smoothed dataset. From the samplewise errors, we 584 can tell that the invariant-based and structure informed models 585 outperform PG-IFNO mostly on sets 6 and 7—which are the protocols on the small deformation regime. As we mentioned before, those sets are differ greatly from the training set, it's expected that neural operator would be less accurate. On the set where 589

00000-6 / Vol. 00, MONTH 2022

Transactions of the ASME

551

590

591

593

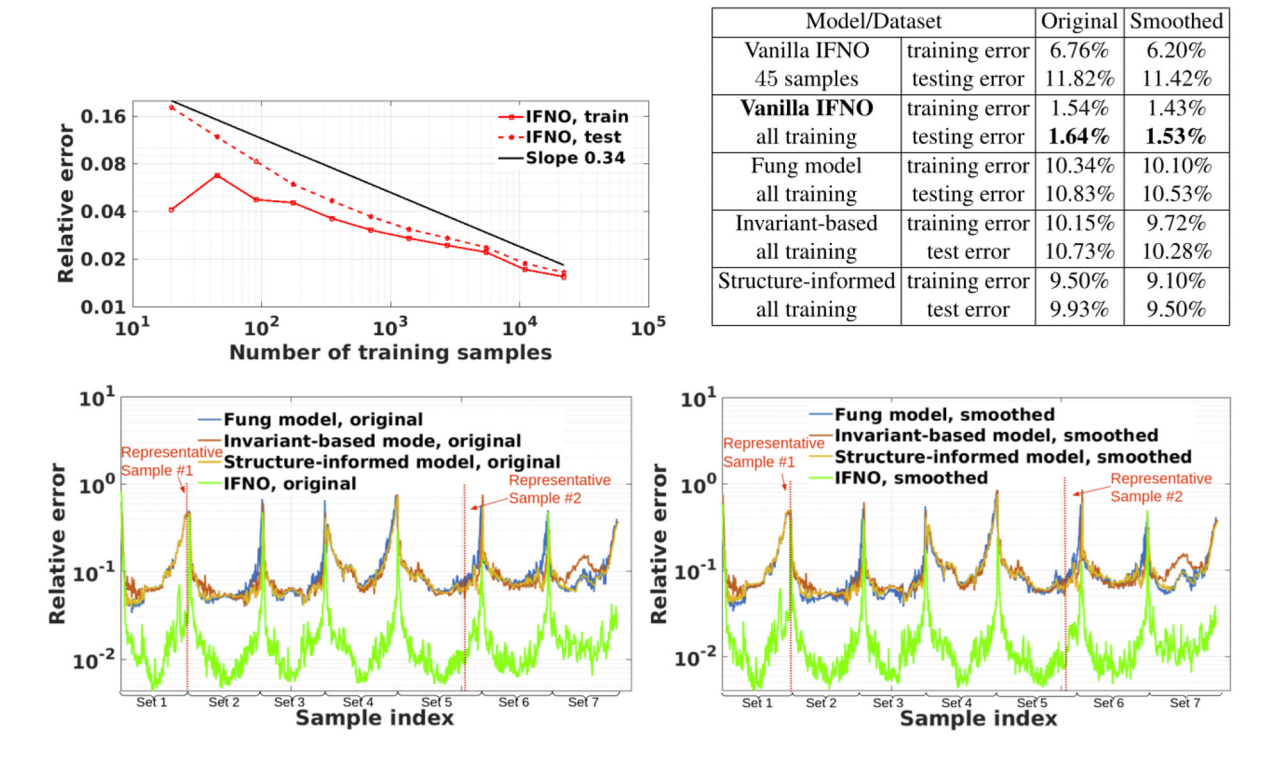


Fig. 3 Error comparisons of different models—study 1: in-distribution prediction with training set on 83% of randomly selected samples. Top: relative errors for the displacement field prediction on the training and test datasets. Left: errors when using different amounts of (original) training samples in the IFNO model. Right: results of the IFNO using 45 training samples and all training samples, and their comparison with three baseline models using all training samples. We highlight the model with the best prediction accuracy in bold. Bottom: samplewise error comparison on all biaxial testing protocol sets. Results from the original dataset are on left and results from the smoothed dataset are on right.

deformation is closer to the training set, i.e., set 3 and set 5, the PG-IFNO model shows a similar or even better performance than the baseline models. This fact is verified by the solutions and prediction errors on a representative sample in set 5, as depicted in

Fig. 6. Compared with structure-informed method, the PG-IFNO 594 model has a lower solution error and captures the material heterogeneity. Hence, these results suggest that sufficient coverage of 596 sample distribution in the training protocol is critical for neural 597

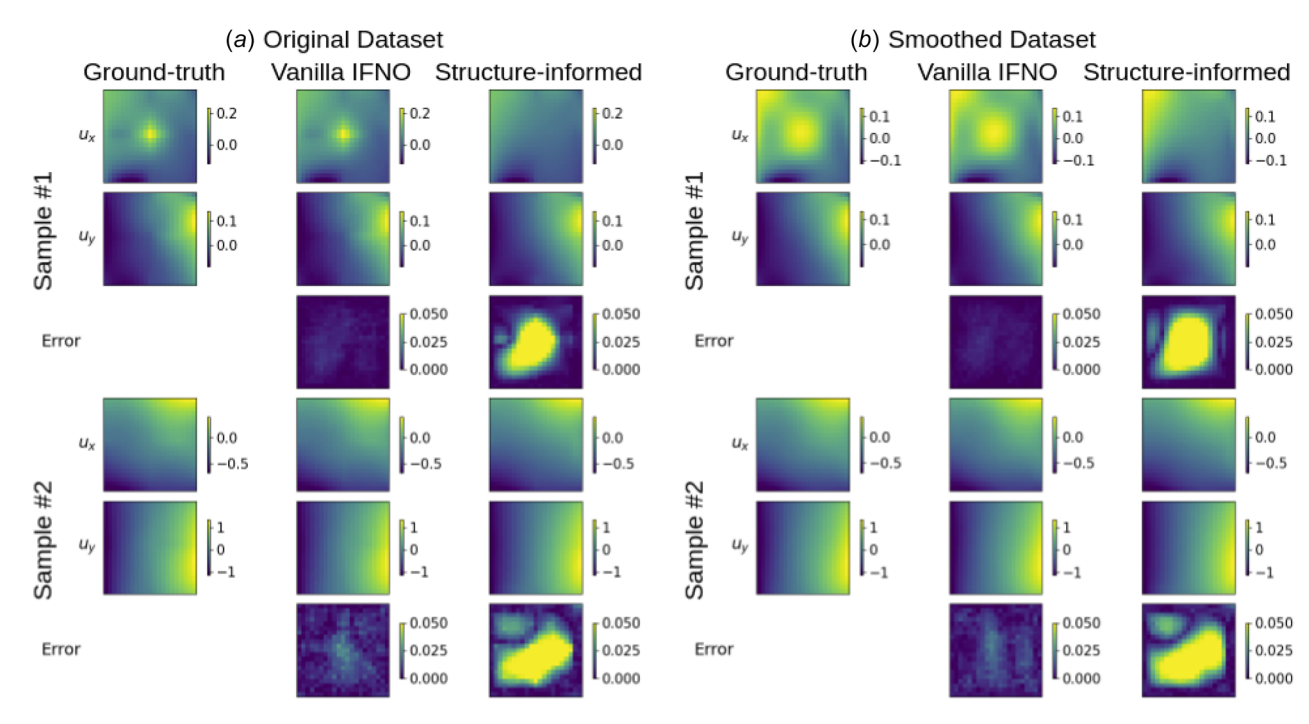


Fig. 4 Visualization of the most accurate baseline constitutive model fitting and IFNO performances on two representative test samples in (a) the original dataset and (b) the smoothed dataset—study 1 (corresponding to the two representative test samples highlighted in Fig. 3—bottom)

**Journal of Biomechanical Engineering** 

MONTH 2022, Vol. 00 / 000000-7

Train on sets 1, 2, 4, test on sets 3, 5, 6, 7			
Model/Dat	Model/Dataset		Smoothed
Vanilla IFNO	training error	1.53%	1.51%
vaiiilla II NO	testing error	16.78%	18.80%
PG-IFNO	training error	1.51%	1.50%
ro-irno	testing error	15.32%	15.76%
Fung model	training error	12.37%	12.54%
Tung moder	testing error	16.80%	15.70%
Invariant-based	training error	12.84%	10.40%
model	testing error	12.98%	9.42%
Structure-informed	training error	10.58%	10.24%
model	testing error	8.76%	8.32%

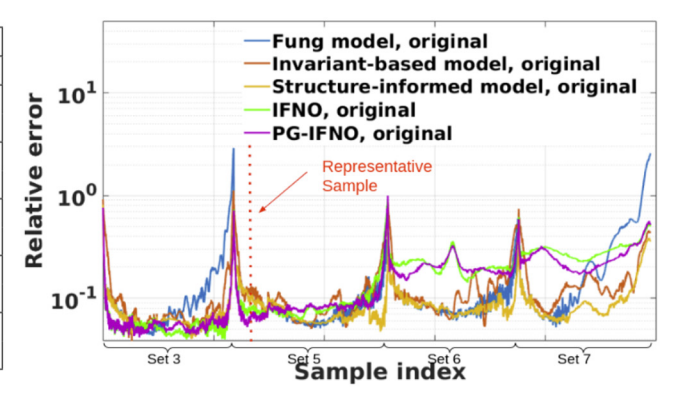


Fig. 5 Error comparisons of different models-study 2: out-of-distribution prediction on the small deformation regime. Left: relative errors for the displacement field prediction on the training and test datasets. We highlight the model with the best prediction accuracy in bold. Right: samplewise error comparison on all test sets from the original (unsmoothed) dataset.

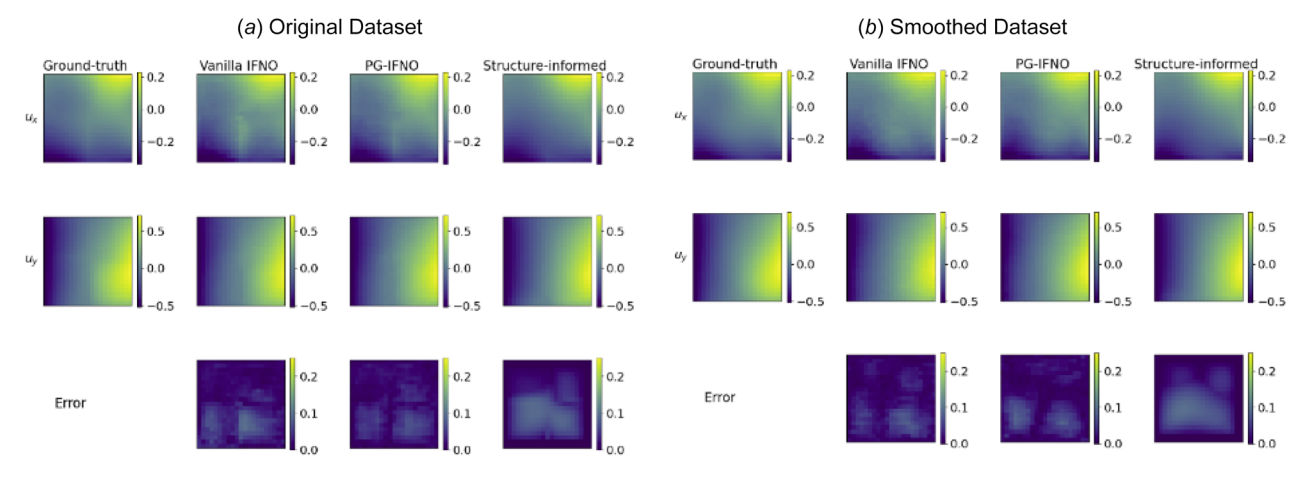


Fig. 6 Visualization of IFNO and PG-IFNO performances on a test sample in (a) the original dataset and (b) the smoothed dataset—study 2 (corresponds to the representative test sample defined in Fig. 5—right)

Train on sets 1, 6, 7, test on 2-5			
Model/Dataset		Smoothed	
training error	1.51%	1.43%	
testing error	8.03%	8.09%	
training error	1.47%	1.35%	
testing error	8.75%	9.08%	
training error	15.49%	14.48%	
testing error	11.75%	11.33%	
training error	14.23%	10.79%	
test error	12.20%	9.29%	
Structure-informed training error		9.73%	
test error	9.18%	8.76%	
	training error testing error training error testing error training error	training error testing error test error 12.20% training error 10.12%	

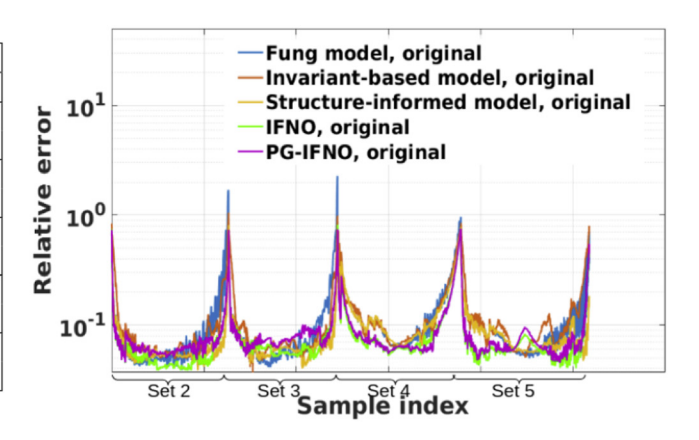


Fig. 7 Error comparisons of different models-study 3: out-of-distribution prediction on the intermediate deformation regime. Left: relative errors for the displacement field prediction on the training and test datasets. We highlight the model with the best prediction accuracy in bold. Right: samplewise error comparison on all test sets from the original (unsmoothed) dataset.

operator learning methods. Even though the constitutive modeling approach can have the lower solution error if the predefined model form exhibits good generalizability like the invariant-based or structured-informed model, the neural operator approach is superior at capturing the heterogeneous features. On these challenging extrapolative learning tasks, incorporating proper physics constraints seems to make the neural operator learning more versatile.

4.3 Study 3: Out-of-Distribution Prediction on the Inter- 605 mediate Deformation Regime. In this study, protocol sets 1, 6, 606 and 7 were used in model training, while the rest of sets (protocols 607 2-5) were for prediction validation. As such, the prediction sets 608 are still with unseen tension ratios from the training sets, but the 609 deformation range of the testing protocols is within the range of 610 the training ones. In Fig. 7 (left), the relative displacement errors 611

00000-8 / Vol. 00, MONTH 2022

599

600

602

603

615

616

617

618 619

620

621

622

623

624

625

626

627

628

629

630

631

632

633

634

635

636

637

638

639

640

641

642

643

644

646

647

648

649

650

651

652

653

654

656

Train on sets 2-7, test on 1			
Model/Da	Model/Dataset		Smoothed
Vanilla IFNO	training error	1.43%	1.38%
vaiilla IFNO	testing error	13.07%	14.05%
PG-IFNO	training error	2.08%	1.36%
FG-IFNO	testing error	15.90%	14.54%
Fung model	training error	15.07%	14.26%
rung moder	testing error	10.34%	10.40%
Invariant-based	training error	12.79%	10.48%
model	test error	12.49%	11.21%
Structure-informed	training error	9.41%	8.96%
model	test error	10.48%	10.41%

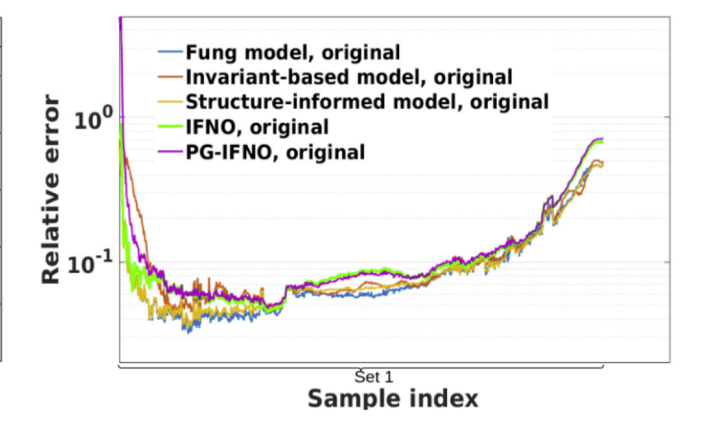


Fig. 8 Error comparisons of different models—study 4: out-of-distribution prediction on the *large* deformation regime. Left: relative errors for displacement field prediction on the training and test datasets. We highlight the model with the best prediction accuracy in bold. Right: samplewise error comparison on all test sets from the original (unsmoothed) dataset.

are provided. We can see that the testing errors from the IFNOs are still much larger than their respective training errors, due to the out-of-distribution learning nature of this study. However, the prediction error from the IFNOs outperforms all three constitutive models by at least 1.15% and 0.67% on the original and smoothed dataset, respectively. Therefore, as long as the dataset has sufficient coverage of the deformation, neural operator learning methods can be a more effective approach than the traditional constitutive models, even in the more challenging out-ofdistribution tasks. To provide further insights into this comparison, Fig. 7 (right) depicts the samplewise errors on the original (unsmoothed) dataset. One can see that the prediction errors are almost uniform among all protocol sets. In this study, the PG-IFNO does not substantially improve the prediction accuracy compared with the original IFNO, possibly because the physics constraint stems from the zero loading case and is more helpful in guiding the prediction in small deformation regimes.

**4.4 Study 4: Out of Distribution Prediction on the Large Deformation Regime.** In the last comparative study scenario, the experimental protocol for prediction was selected to be the one with the largest maximum tension, with the aim to evaluate the models' extrapolative prediction abilities on the large deformation regime. From Fig. 8, one can see that while the IFNO becomes less effective on both datasets, the Fung-type model exhibits a better fit to both the original and smoothed testing datasets. On the other hand, the physics constraint does not help much in this study. These results suggest that to ensure reliable predictions from neural operator learning methods, with an insufficient coverage of deformation range in the training protocols, a judiciously designed physics constraint for the data range becomes important.

#### 5 Conclusion

In this work, we have applied the neural operator learning method to modeling the mechanical responses of a biological tissue specimen under different loading conditions. Specifically, a data-driven computing workflow has been proposed, which learns the material model directly from the DIC displacement tracking measurements and integrates material identification, modeling procedures, and material response prediction into one unified learning framework. With the proposed neural operator learning, the mechanical response of this tissue specimen can be modeled as a data-driven solution operator from the boundary loading to the resultant displacement field, and the learned model will be applicable to unseen loading conditions. To verify its efficacy on real-world soft tissue response learning tasks which feature spatial heterogeneity, measurement noise, anisotropic and nonlinear behaviors, we have used the proposed workflow to model a

porcine heart TVAL specimen with the DIC measurement data 658 collected from biaxial and constrained uniaxial tension tests. In 659 the in-distribution validation case, our proposed neural operator 660 learning method has been shown to significantly outperform the 661 conventional constitutive modeling approach, with its predictions 662 on out-of-distribution learning tasks being less effective. To 663 improve the model generalizability on out-of-distribution tasks, we have further leveraged the neural operator learning method toward physically consistent predictions for tissue at rest and proposed a physics-guided neural operator learning approach. 667 Numerical studies have demonstrated substantial improvements in 668 terms of enhanced generalization performance in the small defor- 669 mation regime. On the other hand, once the network is fully 670 trained, the prediction of displacement field under a new and 671 unseen loading only requires a forward pass in the neural operator 672 model. When tested on a single CPU core, on average it only takes 673 0.012 s for the neural operator to predict one sample of the displacement field, while the same task takes 0.537 s in the baseline 675 finite element solver. Hence, these results suggest that with sufficient coverage of training sample distribution and/or properly 677 designed physics constraints, the neural operator learning 678 approach could offer an alternative approach that outperforms the 679 conventional phenomenological model in complex and heterogeneous material modeling tasks on both accuracy and efficiency.

Despite the encouraging results presented herein, numerous 682 questions and potentials require further investigation. For example, although the proposed no-permanent-deformation constraint 684 seems effective in the small deformation regime, it has little 685 impact on improving the prediction accuracy of the large deformation regimes. As a natural extension, we will consider the 687 enforcement of other physics constraints, which would potentially 688 further enhance the performance of the method's extrapolative 689 predictivity. Another natural future extension to be considered is 690 the generalizability to other specimens with a different computational domain and/or microstructure. We point out that in this 692 work, the neural operator model is trained by assuming that the 693 tissue has unchanged microstructure, geometry, and biomechani- 694 cal properties, leading to the constantly learned network parame- 695 ter  $\theta$ . To achieve the generalizability across different specimens, 696 one possible approach is to consider varying  $\theta$  across different 697 geometries and microstructures and adapt the model using transfer-learning techniques such as the metalearning methods 699 proposed in Ref. [63]. Similarly, translating the currently trained 700 model to whole organ simulations would be another interesting 701 generalization problem. On the other hand, another important next 702 step is to consider other boundary loading scenarios in our learn- 703 ing framework, such as the traction loading problems as demonstrated in the synthetic dataset example in [22]. Moreover, in this 705 considered the three homogeneous 706 study, we have

Journal of Biomechanical Engineering

MONTH 2022, Vol. 00 / 000000-9

phenomenological models: Fung-type, invariant-based, and 708 structure-informed models as the baseline constitutive modeling, 709 because of their popularity and proven efficacy in soft tissue modeling [1,64,65]. However, we would also like to point out that by 711 considering other constitutive models, such as the Holzapfel 712 model [66], and/or incorporating the material microstructure into the conventional model, one might further improve the accuracy of the conventional constitutive model. Finally, another question 715 arises from the possibility of achieving improved performance by optimizing the penalty parameter  $\boldsymbol{\gamma}$  in the physics-guided hybrid 717 loss function (2.5). It has been shown that an optimized penalty 718 parameter could further enhance the accuracy and trainability of 719 the constrained neural networks (see, e.g., Refs. [67–69]). Hence, the performance of PG-IFNO might get further enhanced by designing effective algorithms which select appropriate weights in the hybrid loss function.

#### Acknowledgment 723

724

726

727

728

729

730

731

734

737

738

739

740

741

745

746

747

748

749

760

AQ7

H. You and Y. Yu would like to acknowledge support from the National Science Foundation under award DMS 1753031 and the AFOSR grant FA9550-22-1-0197. Portions of this research were conducted on Lehigh University's Research Computing infrastructure partially supported by NSF Award 2019035. C. Ross, C.-H. Lee, and M.-C. Hsu would like to acknowledge support from the Presbyterian Health Foundation Team Science Grant. C. Ross was in part supported by the National Science Foundation Graduate Research Fellowship Program (GRF2020307284). M.-C. Hsu was in part supported by the National Institutes of Health under award number R01HL142504.

#### **Funding Data**

- Air Force Office of Scientific Research (Grant No. FA9550-22-1-0197; Funder ID: 10.13039/100000181).
- National Institutes of Health (Grant No. R01HL142504; Funder ID: 10.13039/100000002).
- National Science Foundation (Grant Nos. DMS 1753031, 2019035. GRF2020307284; Funder ID: 10.13039/ 100000001).
- Presbyterian Health Foundation (Team Science Grant; Funder ID: ■).

#### References

- [1] Fung, Y., Fronek, K., and Patitucci, P., 1979, "Pseudoelasticity of Arteries and the Choice of Its Mathematical Expression," Am. J. Physiol. Heart Circ. Physical Physiol. Heart Circ. Physical Physiol ol., **237**(5), pp. H620–H631.
- [2] Pant, A. D., Dorairaj, S. K., and Amini, R., 2018, "Appropriate Objective Functions for Quantifying Iris Mechanical Properties Using Inverse Finite Element Modeling," ASME J. Biomech. Eng., 140(7), p. 074502.
- [3] May-Newman, K., and Yin, F., 1998, "A Constitutive Law for Mitral Valve Tissue," ASME J. Biomech. Eng., **120**(1), pp. 38–47.
- [4] Prot, V., Skallerud, B., and Holzapfel, G., 2007, "Transversely Isotropic Membrane Shells With Application to Mitral Valve Mechanics. Constitutive Modelling and Finite Element Implementation," Int. J. Numer. Methods Eng., 71(8), pp. 987-1008.
- [5] Sacks, M. S., Zhang, W., and Wognum, S., 2016, "A Novel Fibre-Ensemble Level Constitutive Model for Exogenous Cross-Linked Collagenous Tissues,' 751 Interface Focus, 6(1), p. 20150090.
  - [6] van den Broek, C. N., Van der Horst, A., Rutten, M., and Van De Vosse, F. N., 2011, "A Generic Constitutive Model for the Passive Porcine Coronary Artery," Biomech. Model. Mechanobiol., 10(2), pp. 249-258
- [7] Bischoff, J. E., Arruda, E. M., and Grosh, K., 2000, "Finite Element Modeling of Human Skin Using an Isotropic, Nonlinear Elastic Constitutive Model," J. 755 Biomech., 33(6), pp. 645-652.
  - [8] Lee, C.-H., Amini, R., Gorman, R. C., Gorman, J. H., III, and Sacks, M. S., 2014, "An Inverse Modeling Approach for Stress Estimation in Mitral Valve Anterior Leaflet Valvuloplasty for In-Vivo Valvular Biomaterial Assessment," J. Biomech., 47(9), pp. 2055–2063.
  - [9] He, O., Laurence, D. W., Lee, C.-H., and Chen, J.-S., 2021, "Manifold Learning Based Data-Driven Modeling for Soft Biological Tissues," J. Biomech., 117, p. 110124.

[10] Lee, C.-H., Zhang, W., Feaver, K., Gorman, R. C., Gorman, J. H., and Sacks, M. S., 2017, "On the In Vivo Function of the Mitral Heart Valve Leaflet: Insights Into Tissue-Interstitial Cell Biomechanical Coupling," Biomech. Model. Mechanobiol., 16(5), pp. 1613–1632.

Total Pages: 12

- [11] Pfeiffer, M., Riediger, C., Weitz, J., and Speidel, S., 2019, "Learning Soft Tissue Behavior of Organs for Surgical Navigation With Convolutional Neural Networks," Int. J. Comput. Assist. Radiol. Surg., **14**(7), pp. 1147–1155.
  [12] He, X., He, Q., and Chen, J.-S., 2021, "Deep Autoencoders for
- Nonlinear Physics-Constrained Data-Driven Computational Framework With Application to Biological Tissue Modeling," AAAI Spring Symposium, MLPS,
- [13] Tac, V., Sree, V. D., Rausch, M. K., and Tepole, A. B., 2021, "Data-Driven Modeling of the Mechanical Behavior of Anisotropic Soft Biological Tissue,' arXiv preprint arXiv:2107.05388, ■

768

774

776

778

783

785

786

788

792

796

798

803

804

805

806

809 810 **AQ10** 

AQ11

814 AQ12

AQ8

- [14] Miñano, M., and Montáns, F. J., 2018, "WYPiWYG Damage Mechanics for Soft Materials: A Data-Driven Approach," Arch. Comput. Methods Eng., 25(1), pp. 165-193.
- [15] Howell, B., and McIntyre, C. C., 2017, "Role of Soft-Tissue Heterogeneity in Computational Models of Deep Brain Stimulation," Brain Stimul., 10(1), pp.
- [16] Wang, K., and Sun, W., 2018, "A Multiscale Multi-Permeability Poroplasticity Model Linked by Recursive Homogenizations and Deep Learning," Comput. Methods Appl. Mech. Eng., 334, pp. 337–380.
- [17] He, Q., Barajas-Solano, D., Tartakovsky, G., and Tartakovsky, A. M., 2020, "Physics-Informed Neural Networks for Multiphysics Data Assimilation With Application to Subsurface Transport," Adv. Water Resour., 141, p. 103610.
- Tartakovsky, A. M., Marrero, C. O., Perdikaris, P., Tartakovsky, G. D., and Barajas-Solano, D., 2020, "Physics-Informed Deep Neural Networks for Learning Parameters and Constitutive Relationships in Subsurface Flow Problems,' Water Resour. Res., **56**(5) p. e2019WR026731.
- [19] Liu, Z., Wu, C., and Koishi, M., 2019, "A Deep Material Network for Multiscale Topology Learning and Accelerated Nonlinear Modeling of Heterogeneous Materials," Comput. Methods Appl. Mech. Eng., 345, pp. 1138–1168.
- Yang, H., Guo, X., Tang, S., and Liu, W. K., 2019, "Derivation of Heterogeneous Material Laws Via Data-Driven Principal Component Expansions," Comput. Mech., 64(2), pp. 365–379.
- [21] Garbrecht, K., Aguilo, M., Sanderson, A., Rollett, A., Kirby, R. M., and Hochhalter, J., 2021, "Interpretable Machine Learning for Texture-Dependent Constitutive Models With Automatic Code Generation for Topological Optimization," Integr. Mater. Manuf. Innov., 10(3), pp. 373-392.
- [22] You, H., Zhang, Q., Ross, C. J., Lee, C.-H., and Yu, Y., 2022, "Learning Deep 789 Implicit Fourier Neural Operators (IFNOs) With Applications to Heterogeneous 790
- Material Modeling," Comput. Methods Appl. Mech. Eng., 398, p. 115296.
  [23] Lu, L., Jin, P., and Karniadakis, G. E., 2019, "Deeponet: Learning Nonlinear Operators for Identifying Differential Equations Based on the Universal Approximation Theorem of Operators," arXiv preprint arXiv:1910.03193, ■
- [24] Lu, L., Jin, P., Pang, G., Zhang, Z., and Karniadakis, G. E., 2021, "Learning Nonlinear Operators Via DeepONet Based on the Universal Approximation Theorem of Operators," Nat. Mach. Intell., 3(3), pp. 218–229.
- [25] Li, Z., Kovachki, N., Azizzadenesheli, K., Liu, B., Bhattacharya, K., Stuart, A., and Anandkumar, A., 2020, "Neural Operator: Graph Kernel Network for Partial Differential Equations," arXiv preprint arXiv:2003.03485, ■
- [26] Li, Z., Kovachki, N., Azizzadenesheli, K., Liu, B., Stuart, A., Bhattacharya, K. and Anandkumar, A., 2020, "Multipole Graph Neural Operator for Parametric Partial Differential Equations," Adv. Neural Inf. Process. Syst., 33(■), ■.
- [27] Li, Z., Kovachki, N. B., Azizzadenesheli, K., Bhattacharya, K., Stuart, A. Anandkumar, A., et al., 2020, "Fourier Neural Operator for Parametric Partial Differential Equations," International Conference on Learning Representations,
- [28] Yin, M., Ban, E., Rego, B. V., Zhang, E., Cavinato, C., Humphrey, J. D., and Em Karniadakis, G., 2022, "Simulating Progressive Intramural Damage Leading to Aortic Dissection Using DeepONet: An Operator–Regression Neural Network," J. R. Soc. Interface, 19(187), p. 20210670.
- [29] Goswami, S., Yin, M., Yu, Y., and Karniadakis, G. E., 2022, "A Physics-Informed Variational DeepONet for Predicting Crack Path in Quasi-Brittle Materials," Comput. Methods Appl. Mech. Eng., 391, p. 114587.
- [30] Yin, M., Zhang, E., Yu, Y., and Karniadakis, G. E., 2022, "Interfacing Finite Elements With Deep Neural Operators for Fast Multiscale Modeling of Mechanics Problems," Comput. Methods Appl. Mech. Eng., ■(■), p. 115027. 808
- [31] Lu, L., Meng, X., Cai, S., Mao, Z., Goswami, S., Zhang, Z., and Karniadakis, G. E., 2021, "A Comprehensive and Fair Comparison of Two Neural Operators Practical Extensions) Based on Fair Data," arXiv:2111.05512, ■
- [32] Guo, X., Li, W., and Iorio, F., 2016, "Convolutional Neural Networks for Steady Flow Approximation," Proceedings of the 22nd ACM SIGKDD International Conference on Knowledge Discovery and Data Mining, ■, ■, pp. 481-490
- and Zabaras, N., 2018, "Bayesian Deep Convolutional Encoder-Decoder Networks for Surrogate Modeling and Uncertainty Quantification," J. Comput. Phys., 366, pp. 415-447.
- Adler, J., and Öktem, O., 2017, "Solving Ill-Posed Inverse Problems Using Iterative Deep Neural Networks," Inverse Probl., 33(12), p. 124007.
- [35] Bhatnagar, S., Afshar, Y., Pan, S., Duraisamy, K., and Kaushik, S., 2019, "Prediction of Aerodynamic Flow Fields Using Convolutional Neural Networks," Comput. Mech., 64(2), pp. 525–545. [36] Khoo, Y., Lu, J., and Ying, L., 2021, "Solving Parametric PDE Problems With
- 820 Artificial Neural Networks," Eur. J. Appl. Math., 32(3), pp. 421–435.

000000-10 / Vol. 00, MONTH 2022

AO13

823

824

840

841

843

844

845

846

847

849

850

[37] You, H., Yu, Y.,	D'Elia, M., Gao, T., a	nd Silling, S., 202	22, "Nonlocal Kernel
Network (NKN):	a Stable and Resolutio	n-Independent De	ep Neural Network,"
arXiv preprint arX	Xiv:2201.02217, ■.		

- [38] LeVeque, R. J., 2007, Finite Difference Methods for Ordinary and Partial Differential Equations: Steady-State and Time-Dependent Problems, SIAM, ■.
- [39] Zienkiewicz, O. C., Taylor, R. L., Nithiarasu, P., and Zhu, J., 1977, The Finite Element Method, Vol. 3, McGraw-Hill, London.
- 825 [40] Karniadakis, G., and Sherwin, S., 2005, Spectral/HP Element Methods for Computational Fluid Dynamics, OUP Oxford, 

  ...
- [41] Raissi, M., Perdikaris, P., and Karniadakis, G. E., 2019, "Physics-Informed Neural Networks: A Deep Learning Framework for Solving Forward and Inverse Problems Involving Nonlinear Partial Differential Equations," J. Comput. Phys., 378, pp. 686–707.
- [42] Weinan, E., and Yu, B., 2018, "The Deep Ritz Method: A Deep Learning-Based Numerical Algorithm for Solving Variational Problems," Commun. Math. Stat., 6(1), pp. 1–12.
- [43] Bar, L., and Sochen, N., 2019, "Unsupervised Deep Learning Algorithm for PDE-Based Forward and Inverse Problems," arXiv preprint arXiv:1904.05417, ■.
- [44] Smith, J. D., Azizzadenesheli, K., and Ross, Z. E., 2021, "Eikonet: Solving the Eikonal Equation With Deep Neural Networks," IEEE Trans. Geosci. Remote Sensing, 59(12), pp. 10685–10696.
- [45] Pan, S., and Duraisamy, K., 2020, "Physics-Informed Probabilistic Learning of Linear Embeddings of Nonlinear Dynamics With Guaranteed Stability," SIAM J. Appl. Dyn. Syst., 19(1), pp. 480–509.
- [46] Agarap, A. F., 2018, "Deep Learning Using Rectified Linear Units (ReLU)," arXiv preprint arXiv:1803.08375, ■.
- [47] Haber, E., Ruthotto, L., Holtham, E., and Jun, S.-H., 2018, "Learning Across
   Scales—Multiscale Methods for Convolution Neural Networks," Proceedings
   of AAAI Conference Artificial Intelligence, 32, ■, ■.
  - [48] Modersitzki, J., 2009, FAIR: Flexible Algorithms for Image Registration, Siam,

    .
  - [49] Ross, C. J., Laurence, D. W., Richardson, J., Babu, A. R., Evans, L. E., Beyer, E. G., Childers, R. C., Wu, Y., Towner, R. A., Fung, K.-M., Mir, A., Burkhart, H. M., Holzapfel, G. A., and Lee, C.-H., 2019, "An Investigation of the Glycosaminoglycan Contribution to Biaxial Mechanical Behaviours of Porcine Atrioventricular Heart Valve Leaflets," J. R. Soc. Interface, 16(156), p. 20190069.
  - [50] Laurence, D., Ross, C., Jett, S., Johns, C., Echols, A., Baumwart, R., Towner, R., Liao, J., Bajona, P., Wu, Y., and Lee, C.-H., 2019, "An Investigation of Regional Variations in the Biaxial Mechanical Properties and Stress Relaxation Behaviors of Porcine Atrioventricular Heart Valve Leaflets," J. Biomech., 83, pp. 16–27.
- [51] Zhang, D. S., and Arola, D. D., 2004, "Applications of Digital Image Correlation to Biological Tissues." J. Biomed. Opt., 9(4), pp. 691–699.
  - tion to Biological Tissues," J. Biomed. Opt., 9(4), pp. 691–699.

    [52] Lionello, G., and Cristofolini, L., 2014, "A Practical Approach to Optimizing the Preparation of Speckle Patterns for Digital-Image Correlation," Meas. Sci. Technol., 25(10), p. 107001.
- [53] Palanca, M., Tozzi, G., and Cristofolini, L., 2016, "The Use of Digital Image Correlation in the Biomechanical Area: A Review," Int. Biomech., 3(1), pp. 1–21.

- [54] Jett, S., Laurence, D., Kunkel, R., Babu, A. R., Kramer, K., Baumwart, R., Towner, R., Wu, Y., and Lee, C.-H., 2018, "An Investigation of the Anisotropic Mechanical Properties and Anatomical Structure of Porcine Atrioventricular Heart Valves," J. Mech. Behav. Biomed. Mater., 87, pp. 155–171.
- [55] Belytschko, T., Krongauz, Y., Organ, D., Fleming, M., and Krysl, P., 1996, "Meshless Methods: An Overview and Recent Developments," Comput. Methods Appl. Mech. Eng., 139(1–4), pp. 3–47.
- [56] Chen, J.-S., Pan, C., Wu, C.-T., and Liu, W. K., 1996, "Reproducing Kernel Particle Methods for Large Deformation Analysis of Non-Linear Structures," Comput. Methods Appl. Mech. Eng., 139(1–4), pp. 195–227.
  [57] Johnson, E. L., Laurence, D. W., Xu, F., Crisp, C. E., Mir, A., Burkhart, H. M.,
- [57] Johnson, E. L., Laurence, D. W., Xu, F., Crisp, C. E., Mir, A., Burkhart, H. M., Lee, C.-H., and Hsu, M.-C., 2021, "Parameterization, Geometric Modeling, and Isogeometric Analysis of Tricuspid Valves," Comput. Methods Appl. Mech. Eng., 384, p. 113960.
   862
- [58] Kamensky, D., Xu, F., Lee, C.-H., Yan, J., Bazilevs, Y., and Hsu, M.-C., 2018,
   "A Contact Formulation Based on a Volumetric Potential: Application to Isogeometric Simulations of Atrioventricular Valves," Comput. Methods Appl.
   Mech. Eng., 330, pp. 522–546.
- [59] Fan, R., and Sacks, M. S., 2014, "Simulation of Planar Soft Tissues Using a Structural Constitutive Model: Finite Element Implementation and Validation,"
   J. Biomech., 47(9), pp. 2043–2054.
- [60] Lee, C.-H., Rabbah, J.-P., Yoganathan, A. P., Gorman, R. C., Gorman, J. H., and Sacks, M. S., 2015, "On the Effects of Leaflet Microstructure and Constitutive Model on the Closing Behavior of the Mitral Valve," Biomech. Model. Mechanobiol., 14(6), pp. 1281–1302.

868

869

870

879

880

882

- [61] Price, K., Storn, R. M., and Lampinen, J. A., 2006, Differential Evolution: A Practical Approach to Global Optimization, Springer Science & Business Media, .
- [62] Abaqus, G., 2011, Abaqus 6.11, Dassault Systemes Simulia Corporation, Providence, RI.
- [63] Zhang, L., You, H., and Yu, Y., 2022, "Metanor: A Meta-Learnt Nonlocal Operator Regression Approach for Metamaterial Modeling," arXiv preprint arXiv:2206.02040, ■.
  875
- [64] Sun, W., and Sacks, M. S., 2005, "Finite Element Implementation of a Generalized Fung-Elastic Constitutive Model for Planar Soft Tissues," Biomech. Model. Mechanobiol., 4(2–3), pp. 190–199.
- [65] Famaey, N., and Sloten, J. V., 2008, "Soft Tissue Modelling for Applications in Virtual Surgery and Surgical Robotics," Comput. Methods Biomech. Biomed. Eng., 11(4), pp. 351–366.
- [66] Holzapfel, G. A., 2002, "Nonlinear Solid Mechanics: A Continuum Approach for Engineering Science," Meccanica, 37(4/5), pp. 489–490.
- [67] Wang, S., Wang, H., and Perdikaris, P., 2021, "Learning the Solution Operator of Parametric Partial Differential Equations With Physics-Informed Deep-ONets," Sci. Adv., 7(40), p. eabi8605.
- [68] Wang, S., Yu, X., and Perdikaris, P., 2022, "When and Why Pinns Fail to Train: A Neural Tangent Kernel Perspective," J. Comput. Phys., 449, p. 110768.
- [69] McClenny, L., and Braga-Neto, U., 2020, "Self-Adaptive Physics-Informed Neural Networks Using a Soft Attention Mechanism," arXiv preprint arXiv:2009.04544, ■.